

Reflection, Transmission and Diffraction Efficiencies in Homogenous Optical Thin Film and Grating Structures: An Overview

Luc Lévesque¹

¹ Physics Department, Royal Military College of Canada, Kingston, Canada

Correspondence: Luc Lévesque, Physics Department, Royal Military College of Canada, Kingston, Canada.
E-mail: Luc.Levesque@rmc.ca

Received: June 14, 2013 Accepted: June 26, 2013 Online Published: July 30, 2013

doi:10.5539/apr.v5n5p1

URL: <http://dx.doi.org/10.5539/apr.v5n5p1>

Abstract

The matrix formalism is applied to describe various stratified and periodic systems that are used to couple optical energy into a dielectric film or medium. As the literature is often presenting cases for the transverse electric wave (*TE*), general analytical and numerical solutions are reviewed for many types of optical thin film systems with some emphasis on the transverse magnetic (*TM*) wave. This manuscript is divided into two main parts. In the first part, we look at stratified systems formed by a succession of multilayers and also present some applications for this type of optical systems such as bi-layer dielectric stacks. Tunneling across an air gap formed by two prisms' long sides brought close to each other is also presented. Tunneling modes in optical system is reviewed in detail in systems that are probing an optical waveguide layer. In the second part of this manuscript, we are looking at optical systems in which a corrugated surface is used to couple energy into a medium. The matrix formalism used in this second part is applied mostly to grating waveguide structures and used in numerical computation of diffraction efficiencies (*DE*). Binary dielectric and metallic grating are also introduced with some emphasis on general ideas leading to the origin of photonic band-gap. This manuscript is reviewing various applications involving the matrix method supported by some results, but is also meant to be an overview with the main emphasis on optical thin film system grating waveguide structures.

Keywords: homogenous optical thin film, stratified systems, grating waveguide

1. Stratified Systems of Uniform Thin Film

Multilayers have been treated extensively by using the matrix formalism in the literature as early as the 1950's by Abelès (1950 and 1957) and Heavens (1960). The matrix formalism is still very much used nowadays as the method has been proved to be an excellent tool in providing very good results for various applications such as optical constants determinations reported by Lévesque, Paton and Payne (1994), Lévesque (2011a) and Salomon, Macleod and Tollin (1997), in stratified multilayered films spectroscopy demonstrated by Ohta and Ishida (1990), in photonic devices explored by Lévesque and Paton (1994) and Yeh and Yariv (1977), in waveguide devices designed by Lenaerts, Michel, Tilkens, Lion and Renotte (2005), and in grating waveguide structures presented in the works of Lalanne and Morris (1996), Moharam, Grann, Pommet and Gaylord (1995) and Born and Wolf (1980).

1.1 Characteristic Matrix of a Homogeneous Thin Optical Film

An optical thin film is homogeneous if its permittivity $\epsilon (= n^2)$ is equal to a constant throughout the whole material thickness d from which the film is made. In the previous definition of the material permittivity ϵ , n is referred to as the refractive index of the thin film. As the transverse electric (*TE*) wave is often treated in various texts such as Born and Wolf (1980), Hecht (2002), Lévesque (2011a), Haus (1984) and Macleod (2001), the transverse magnetic (*TM*) will be considered. Figure 1(a) illustrates the directions of the E and H field vectors in a homogeneous thin film bounded by two semi-infinite media of refractive index n_1 and n_3 for a *TE* wave. Figure 1(b) depicts the corresponding directions defined in Figure 1(a) for the *TM* wave. Note that all the E -field vectors defined as pointing out the plane of Figure 1(a) keep their direction after a reflection or transmission at both interfaces 1 and 2. To be consistent with the definition of the E -field vectors for the *TE* wave (c.f. Figure 1(a)), all tangential components of the E -field vectors were assumed to be along the same direction in Figure 1(b), that is in the $+y$ -direction. Therefore, at normal incidence, the E -field vectors for both the *TE* and *TM* waves are assumed to keep their direction after a reflection or transmission. Note in Figure 1(b) that all the tangential

components of all the H -field vectors were also assumed to change their direction after a reflection at both interfaces 1 and 2 for consistency with the TE wave arbitrary definition. Consequently, at normal incidence, the H -field vectors for both the TE and TM waves are assumed to reverse their direction after a reflection and keep their direction after a transmission. The vector product $E \times B$ for all corresponding field vectors defined in figure 1 is in the direction of the wave propagation, in accordance with the Poynting vector formulation. For all field vectors we also assumed the dependence $\exp(-j(\vec{k} \cdot \vec{r} - \omega t))$, where $k = 2\pi m/\lambda$ is the propagation vector and ω is the cyclic frequency. In the previous expression λ is the wavelength of the electromagnetic wave in the vacuum.

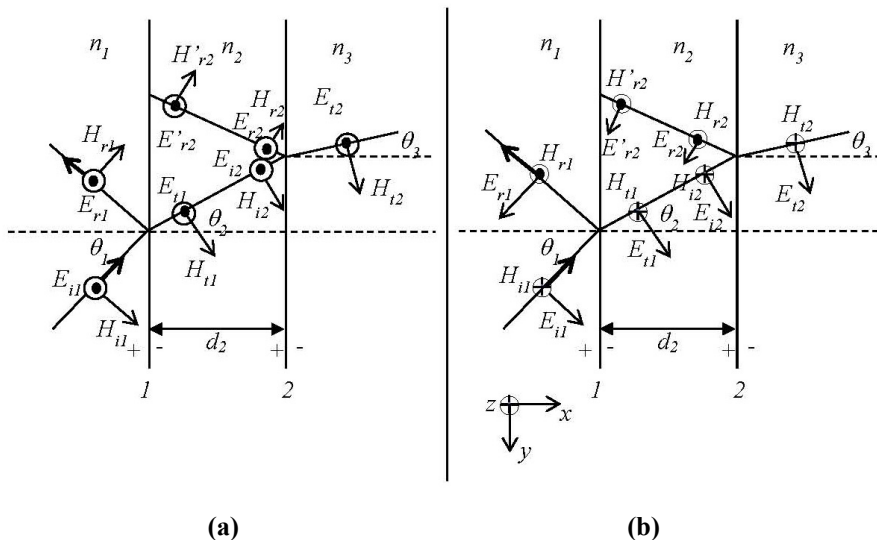


Figure 1. Representation of field vectors for (a) TE and (b) TM waves

The expressions for the tangential components of both the E and H field vectors for the TM wave at each interface in figure 1b are:

$$E_{1y}^+ = (E_{i1} + E_{r1}) \cos \theta_1 \quad E_{1y}^- = (E_{i1} + E'_{r2}) \cos \theta_2$$

$$H_{1z}^+ = \left(\frac{\epsilon_o}{\mu_o}\right)^{1/2} n_1 (E_{i1} - E_{r1}) \quad H_{1z}^- = \left(\frac{\epsilon_o}{\mu_o}\right)^{1/2} n_2 (E_{i1} - E'_{r2}) \tag{1}$$

$$E_{2y}^+ = (E_{i2} + E_{r2}) \cos \theta_2 \quad E_{2y}^- = E_{i2} \cos \theta_3$$

$$H_{2z}^+ = \left(\frac{\epsilon_o}{\mu_o}\right)^{1/2} n_2 (E_{i2} - E_{r2}) \quad H_{2z}^- = \left(\frac{\epsilon_o}{\mu_o}\right)^{1/2} n_3 E_{i2} \tag{2}$$

where superscripts + or - means on the left or right of the interface, respectively. ϵ_o and μ_o in the set of Equations (1) and (2) are the permittivity and permeability of free space, respectively.

The two sets of expressions for the E and H field tangential components at interfaces 1- and 2+ are used to find the characteristic matrix of the thin film. The other two sets will be used later to find the Fresnel coefficients r and t . From the set of equations at interface 1-, we write:

$$\begin{bmatrix} E_{1y}^- \\ H_{1z}^- \end{bmatrix} = \begin{bmatrix} \cos \theta_2 & \cos \theta_2 \\ \left(\frac{\epsilon_o}{\mu_o}\right)^{1/2} n_2 & -\left(\frac{\epsilon_o}{\mu_o}\right)^{1/2} n_2 \end{bmatrix} \begin{bmatrix} E_{i1} \\ E'_{r2} \end{bmatrix} \tag{3}$$

From Figure 1 and phase shift considerations, we can also write that $E_{i2} = E_{i1} \exp(-jk_2 h_2)$ and $E'_{r2} = E_{r2} \exp(-jk_2 h_2)$, where $h_2 = d_2 \cos \theta_2$ and $k_2 = n_2 k_o$, with $k_o = 2\pi/\lambda$. The set of equations at interface 2+ can now be written under the matrix form as:

$$\begin{bmatrix} E_{2y}^+ \\ H_{2z}^+ \end{bmatrix} = \begin{bmatrix} \exp(-jk_2 h_2) \cos \theta_2 & \exp(jk_2 h_2) \cos \theta_2 \\ (\frac{\epsilon_o}{\mu_o})^{1/2} n_2 \exp(-jk_2 h_2) & -(\frac{\epsilon_o}{\mu_o})^{1/2} n_2 \exp(jk_2 h_2) \end{bmatrix} \begin{bmatrix} E_{r1} \\ E_{r2} \end{bmatrix} \quad (4)$$

By inverting the 2×2 matrix in Equation (4), we have:

$$\begin{bmatrix} E_{r1} \\ E_{r2} \end{bmatrix} = \begin{bmatrix} \frac{\exp(jk_2 h_2)}{2 \cos \theta_2} & \frac{\exp(jk_2 h_2)}{2 n_2 (\frac{\epsilon_o}{\mu_o})^{1/2}} \\ \frac{\exp(-jk_2 h_2)}{2 \cos \theta_2} & \frac{-\exp(jk_2 h_2)}{2 n_2 (\frac{\epsilon_o}{\mu_o})^{1/2}} \end{bmatrix} \begin{bmatrix} E_{2y}^+ \\ H_{2z}^+ \end{bmatrix} \quad (5)$$

and replacing the matrix Equation (5) into (3) it can be shown that:

$$\begin{bmatrix} E_{1y}^- \\ H_{1z}^- \end{bmatrix} = \begin{bmatrix} \cos(k_2 h) & j \sin(k_2 h) / Y_2 \\ j Y_2 \sin(k_2 h) & \cos(k_2 h) \end{bmatrix} \begin{bmatrix} E_{2y}^+ \\ H_{2z}^+ \end{bmatrix} \quad (6)$$

The 2×2 matrix in Equation (6) is the characteristic matrix of the homogeneous thin film of thickness d_2 , where

$Y_2 = \frac{n_2 (\frac{\epsilon_o}{\mu_o})^{1/2}}{\cos \theta_2}$. The tangential components of both the E and H field vectors on either sides of the interfaces 1 and 2 are equal and they can be used in matrix Equation (6). Therefore, replacing $E_{1y}^+ = E_{1y}^-$, $E_{2y}^+ = E_{2y}^-$, $H_{1z}^+ = H_{1z}^-$ and $H_{2y}^+ = H_{2y}^-$ into Equation (6), one finds:

$$\begin{bmatrix} (E_{i1} + E_{r1}) \cos \theta_1 \\ (\frac{\epsilon_o}{\mu_o})^{1/2} n_1 (E_{i1} - E_{r1}) \end{bmatrix} = M \begin{bmatrix} E_{t2} \cos \theta_3 \\ (\frac{\epsilon_o}{\mu_o})^{1/2} n_3 E_{t2} \end{bmatrix}. \quad (7)$$

The entries of the characteristic matrix M in Equation (7) are m_{11} , m_{12} , m_{21} and m_{22} and the expression for each of these is given in matrix Equation (6). Defining the reflection and transmission coefficients as $r = E_{r1}/E_{i1}$ and $t = E_{t2}/E_{i1}$, it can be found from Equation (7) that:

$$r = \frac{Y_1 m_{11} + Y_1 Y_3 m_{12} - m_{21} - Y_3 m_{22}}{Y_1 m_{11} + Y_1 Y_3 m_{12} + m_{21} + Y_3 m_{22}} \quad (8)$$

and

$$t = \frac{2(n_1/n_3)Y_3}{Y_1 m_{11} + Y_1 Y_3 m_{12} + m_{21} + Y_3 m_{22}} \quad (9)$$

where $Y_i = \frac{n_i (\frac{\epsilon_o}{\mu_o})^{1/2}}{\cos \theta_i}$ for $i = 1, 2$ or 3 . The reflectance R and transmittance T are then defined by Macleod (2001) and also by Moharam and Gaylord (1981) as:

$$\begin{aligned} R &= r^* r \\ T &= \text{Re} \left(\frac{n_3 \cos \theta_3}{n_1 \cos \theta_1} \right) t^* t \end{aligned} \quad (10)$$

where r^* and t^* mean the complex conjugate of r and t respectively. In the case of ideal dielectrics with real refractive indices n_1 , n_2 or n_3 , the optical energy is partly reflected or transmitted without any dissipation of the energy (absorption) into each material and the sum of the reflectance and transmittance can be shown to be equal to 1 by using Equations (8), (9) and (10).

1.2 Tunneling Across an Air Gap between the Prisms' Long Faces

Tunneling of electromagnetic waves is not often discussed as an application of a thin dielectric bounded by two semi-infinite media. The concept is interesting as it is analogous to a particle penetrating a barrier, which is referred to as tunneling in quantum mechanics in the textbooks by French (1978) and Liboff (1988). The electromagnetic field is evanescent at the interface of two dielectric media for angles of incidence θ_i larger than the critical angle. This means that the E or H fields will decay exponentially within the air gap formed by the prisms' long sides separated by a distance d_2 as shown in Figure 2. The exponential decay also depends upon the wavelength of the electromagnetic radiation incoming from prism 1. As a result, tunneling of the electromagnetic wave is relatively easier to investigate at longer wavelength λ such as microwaves, because the effect can be appreciated over a larger air gap between the prisms' long faces.

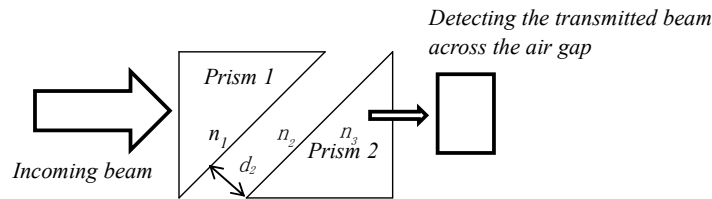


Figure 2. Tunneling of electromagnetic waves across an air gap formed by the long face of two identical right angle prisms

Figure 3 is showing the results of the change in db signal of microwaves entering into prism 1 at $\lambda \sim 33$ mm as d_2 is varied. The db signal is measured as $10 \log(P/P_o)$, where P is the power at a given value of d_2 and P_o is the reference power at $d_2 = 0$. As we set $P = P_o$ at $d_2 = 0$, the db signal is zero at $d_2 = 0$ and the change in db signal is negative as d_2 is varied from $d_2 = 0$. In the set-up in Figure 2, prism 2 is displaced with a micrometer by a small distance in millimeters and the change in power is measured at each value of d_2 . As the system is symmetric and the incident angle θ_i is kept constant at 45° during the experiment, Fresnel losses at both the input and output faces remain the same at each value of d_2 . Therefore, by taking the change in the db signal we cancel Fresnel losses and only the transmittance across the air gap bounded by two semi-infinite media with the same refractive indices of each identical prism is being detected. The transmittance T can also be calculated from Equation (10).

Equation (10) is valid for both TE and TM wave, except we use $Y_i = n_i \left(\frac{\epsilon_o}{\mu_o} \right)^{1/2} \cos \theta_i$ in the case of TE wave. By

assuming that half of the total radiation is TE and the other half is TM , the average is obtained by merely adding the transmittance for TE and TM and then dividing by two. Then we take the logarithm in base 10, the result is multiplied by ten and then the calculation from the matrix method (solid curve in Figure 3) is then compared with the experimental values given by the change in db signal. At small values of d_2 , internal reflections within the air gap are important and they contribute to the transmittance. At larger values of $d_2 > 5$ mm, the internal reflections occurring within the air gap is making less contribution to the transmittance while some energy is leaking into prism 2. As the wave is exponentially decaying with distance, the logarithmic change is expected to be linear with distance at larger d_2 as shown in Figure 3.

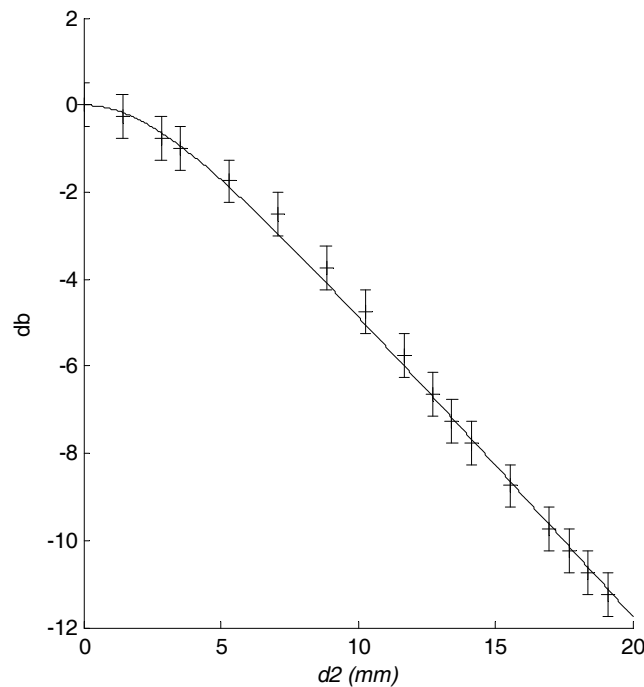


Figure 3. Data points with error bars of the change in db signal for the transmittance as a function of d_2 . The solid line is the change in db calculated from Equation (10). The refractive indices of each prism at $\lambda = 33$ mm is $n_1 = n_3 = 1.85$. The incident angle $\theta_1 = 45^\circ$ was kept constant during the experiment

1.3 Tunneling by Coupling Gap across an Absorbing Thin Film (TM Waves)

Tunneling by coupling gap was used to probe the properties of materials and determine the thickness of a dielectric layer as explored by Podgorsek and Franke (2002), Lévesque, Paton and Payne (1994) and Lévesque and Paton (1997). Let us consider two films bounded by two semi-infinite media as shown in Figure 4. The semi-infinite medium of refractive index n_1 is a prism with a high refractive index. The refractive indices of the films of thicknesses d_2 and d_3 are n_2 and n_3 , respectively. Note that the refractive index of the thin metallic film is complex as it is a conducting medium. A thin metallic film having a thickness d_2 , which is much smaller than the dielectric film thickness d_3 is used as a coupling gap in order to allow tunneling into the dielectric film so that a waveguide mode can be supported. At a given incident angle θ_1 , the incident incoming wave can penetrate across the coupling metal film so that the component of the propagation vector along the y-direction β exactly matches an eigenmode vector of the dielectric waveguide. The number of tunneling dips should increase with the thickness d_3 as more solutions for β are found for larger thickness d_3 . When proper matching of the propagation vector components β occurs, waveguide modes are being supported by the dielectric waveguide and the reflectance drops sharply at that given value of θ_1 . A high refractive index prism is useful to make the field evanescent in the air so that the optical energy can be confined into the dielectric film. The field decays exponentially in the air from the dielectric air interface when the component of the propagation vector along x, k_{4x} becomes a complex value. Assuming Snell's law ($n_1 \sin \theta_1 = n_4 \sin \theta_4$), one writes

$$k_{4x} = n_4 k_o \cos \theta_4 = n_4 k_o (1 - \sin^2 \theta_4)^{1/2} = n_4 k_o \left(1 - \frac{n_1^2 \sin^2 \theta_1}{n_4^2}\right)^{1/2} \quad (11)$$

In Equation (11), $k_o = 2\pi/\lambda$, θ_4 is the angle in the fourth medium (i.e., air) and it can be shown that k_{4x} becomes a complex value for $\theta_1 > \sin^{-1}(n_4/n_1)$.

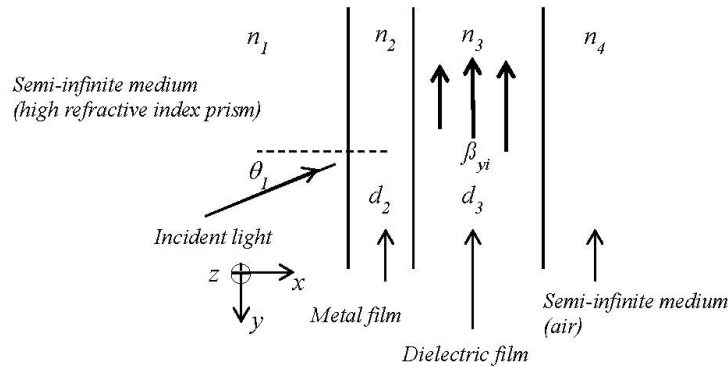


Figure 4. Structure consisting of both the metal and dielectric films bounded by two semi-infinite media. The metal film thickness d_2 is assumed to be much smaller than the dielectric film d_3

By applying the method presented in section *Ii*), it can be shown that the sets of E and H field vectors in the dielectric film can be cast under the same form as Equation (6), that is:

$$\begin{bmatrix} E_{2y}^+ \\ H_{2z}^+ \end{bmatrix} = \begin{bmatrix} \cos(k_3 h_3) & j \sin(k_3 h_3) / Y_3 \\ j Y_3 \sin(k_3 h_3) & \cos(k_3 h_3) \end{bmatrix} \begin{bmatrix} E_{3y}^+ \\ H_{3z}^+ \end{bmatrix} \quad (12)$$

where $h_3 = d_3 \cos \theta_3$ and $Y_3 = n_3 (\frac{\epsilon_o}{\mu_o})^{1/2} / \cos \theta_3$. The 2×2 matrix in Equation (12) is merely the characteristic matrix for the dielectric layer of thickness d_3 . Substituting Equation (12) into Equation (6), one can find:

$$\begin{aligned} \begin{bmatrix} E_{1y}^- \\ H_{1z}^- \end{bmatrix} &= \begin{bmatrix} \cos(k_2 h_2) & j \sin(k_2 h_2) / Y_2 \\ j Y_2 \sin(k_2 h_2) & \cos(k_2 h_2) \end{bmatrix} \begin{bmatrix} \cos(k_3 h_3) & j \sin(k_3 h_3) / Y_3 \\ j Y_3 \sin(k_3 h_3) & \cos(k_3 h_3) \end{bmatrix} \begin{bmatrix} E_{3y}^+ \\ H_{3z}^+ \end{bmatrix} \\ &== M_{23} \begin{bmatrix} E_{3y}^+ \\ H_{3z}^+ \end{bmatrix} \end{aligned} \quad (13)$$

where the product of the 2×2 matrices M_{23} yields the characteristic matrix for the multi-layer formed by both the metal and the dielectric films. This means that the reflectance and transmittance given by Equations (8) and (9) can be used as long as m_{11} , m_{12} , m_{21} and m_{22} are the entries of M_{23} and Y_3 is being replaced by $Y_4 = n_4 (\frac{\epsilon_o}{\mu_o})^{1/2} / \cos \theta_4$. In general, the optical admittance Y_i is expressed as $n_i (\frac{\epsilon_o}{\mu_o})^{1/2} / \cos \theta_i$ and $n_i (\frac{\epsilon_o}{\mu_o})^{1/2} \cos \theta_i$ for the TM and TE waves, respectively. Assuming a high refractive index $n_1 = 2.0$ and $n_4 = 1$ (air) and according to the condition set by Equation (11), waveguide modes can propagate for $\theta_i > 30^\circ$. Equation (8) was used to compute the reflectance for the multi-layer of Figure 4, for $n_1 = 2.0$, $\epsilon_2 = n_2^2 = -18.6 - 0.6j$, $d_2 = 50 \text{ nm}$, $n_3 = 1.5$, $d_3 = 1.5 \mu\text{m}$ and $n_4 = 1$ (air). Figure 5(a) shows the reflectance. Note that 4 reflectance dips at $\theta_i < 50^\circ$ are displaying a very small full width at half maximum (FWHM) and the last reflectivity dip near 53° is broader. As expected, the very first of these four reflectance dips is occurring at incident angles greater than $\sin^{-1}(n_4/n_1)$, that is at $\theta_i > 30^\circ$.

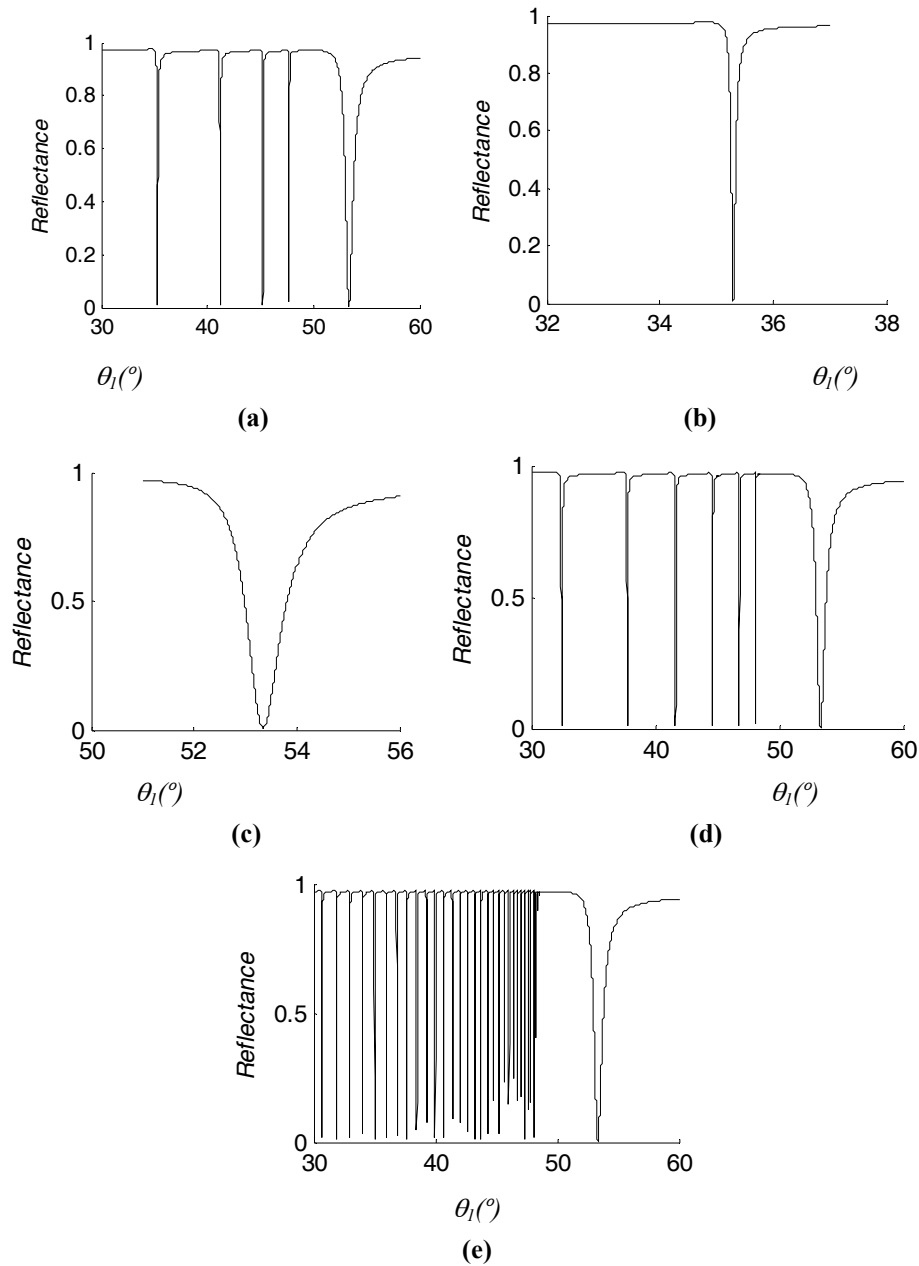


Figure 5. Reflectance for the structure shown in Figure 4 for the *TM* wave (a) Tunneling and SPR dips for a high refractive index prism $n_1 = 2.0$. The following data were used in the computation: $\epsilon_2 = -18.6 - 0.6j$, $d_2 = 50 \text{ nm}$, $n_3 = 1.5$, $d_3 = 1.5 \mu\text{m}$ and $n_4 = 1$ (air). (b) First tunneling dip at an incident angle of 35.3° (c) SPR dip at an incident angle of about 53° (d) Tunneling dips and SPR dip for the multi-layer structure with a high refractive index prism.

The data used in the computation are the same as in part (a) except $d_3 = 2.0 \mu\text{m}$. (e) Tunneling dips for the multi-layer structure with a high refractive index prism. The data used in the computation are the same as in part (a) except $d_3 = 10 \mu\text{m}$

The first four reflectivity dips with small (FWHM) are commonly referred to as tunneling dips and they depend on the real and imaginary parts of the dielectric layer and thickness d_3 . It was shown by Podgorsek and Franke (2002) and Lévesque, Paton and Payne (1994) that the position of these tunneling dips is mostly depending upon the real part of n_3 and the depth depends strongly upon the imaginary part of n_3 . In the computation of the reflectance shown in Figure 5(a) n_3 was assumed to be real. The last reflectance dip with a larger width in Figure 5(a) is referred to as the surface plasmon resonance (SPR) dip discussed extensively in the literature by Burke,

Stegeman and Tamir (1986), Raether (1988), Welford (1991), Wang (2003), Nikolajsen, Leosson and Bozhevolnyi (2004), Homola, Yee and Gauglitz (1999), Matsubara, Kawata and Minami (1988) and Kano and Kawata (1994). The SPR dip is only depending upon the metal properties, that is, ϵ_2 and the metal thickness d_2 . The reflectance SPR dip was also used by Lévesque et al. (1994) and Lévesque (2011b) to estimate the metal permittivity ϵ_2 and determine the metal thickness d_2 . Figures 5(b) and 5(c) are showing the first tunneling and SPR dips, respectively. Note that the FWHM is much smaller for the tunneling dip (c.f. Figure 5b)).

Figures 5(d) and 5(e) show the reflectance of the multi-layer structure for a dielectric layer of 2.5 μm and 10 μm , respectively. Note that the number of tunneling dips is larger for the dielectric layer of 10 μm as more modes can be supported by a larger waveguide film, but the SPR dip always occurs near $\theta_1 \sim 53^\circ$ as it is not depending upon d_3 .

1.4 Bi-Layer Thin Film Stack

By-layer thin films are used as quarter wave dielectric stacks and they were reported by Yeh et al. (1977) and Barnes, Priest, Kitson and Sambles (1996), in multi-layered system to control visible-light by Smith, Fakhouri, Pulpytel and Arefi-Khonsari (2012) or in solar energy material used for solar cells as demonstrated by Tazawa, Okada, Yoshimura and Ikezawa (2004). They also have been used in reflection optical filters, but grating used in guided-mode resonance filters explored by Tibuleac and Magnusson (1997) are performing better and they will be discussed in the next section. The basic structure shown in Figure 4 can be used repeatedly to form the bi-layer film stack shown in Figure 6. To enhance the reflectance in bi-layer stacks, two different dielectric films with low and high refractive indices are often used and they will be referred to as n_L and n_H , respectively. The bi-layer thin-film stack is bounded by two semi-infinite media of refractive indices n_i and n_t .

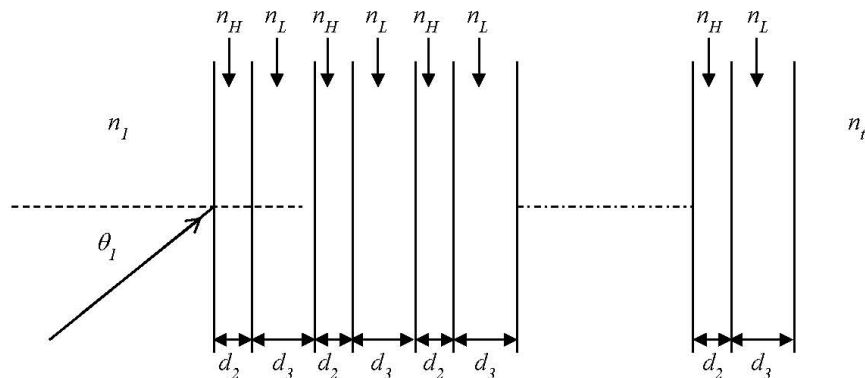


Figure 6. Bi-layer thin-film stack bounded by two semi-infinite media

The basic unit of two consecutive films of thicknesses d_2 and d_3 can be used to treat the bi-layer thin-film stack illustrated in Figure 6. Repeating this basic unit having a total thickness $d (= d_2 + d_3)$ N times, the characteristic matrix of the resulting bi-layer stack $M(Nd)$ is found by the matrix product of each individual unit M_{23} and as a result:

$$M(Nd) = \underbrace{M_{23} M_{23} M_{23} \dots M_{23}}_{N \text{ times}} = (M_{23}(d))^N \quad (14)$$

where M_{23} is the characteristic matrix of one period of thickness d given by Equation (13), that is,

$$M_{23}(d) = \begin{bmatrix} A & B \\ C & D \end{bmatrix} \quad (15)$$

where

$$\begin{aligned}
A &= \cos(\beta_2) \cos(\beta_3) - \frac{Y_3}{Y_2} \sin(\beta_2) \sin(\beta_3) \\
B &= \frac{J}{Y_3} \cos(\beta_2) \sin(\beta_3) + \frac{J}{Y_2} \sin(\beta_2) \cos(\beta_3) \\
C &= jY_2 \sin(\beta_2) \cos(\beta_3) + jY_3 \cos(\beta_2) \sin(\beta_3) \\
D &= \cos(\beta_2) \cos(\beta_3) - \frac{Y_2}{Y_3} \sin(\beta_2) \sin(\beta_3)
\end{aligned} \tag{16}$$

and $\beta_2 = k_2 h_2$ and $\beta_3 = k_3 h_3$.

Note that matrix $M_{23}(d)$ is unimodular as its determinant is equal to 1. The N power of a unimodular matrix $M_{23}(d)$ can be found on a direct proof based on the theory of matrices by Abelès (1950) and Born and Wolf (1980). From this direct proof, it can be shown for N periods of thickness d that:

$$(M(d))^N = \begin{bmatrix} AU_{N-1}(\alpha) - U_{N-2}(\alpha) & BU_{N-1}(\alpha) \\ CU_{N-1}(\alpha) & DU_{N-1}(\alpha) - U_{N-2}(\alpha) \end{bmatrix} \tag{17}$$

where $\alpha = \frac{1}{2}(A + D)$ and $U_N(\alpha) = \frac{\sin[(N+1)\cos^{-1}\alpha]}{(1-\alpha^2)^{1/2}}$, which are referred to as the Chebyshev Polynomials of the second kind. From the previous analysis and definitions, it can be shown that for TE and TM waves:

$$\alpha = \cos^2 \beta - \frac{1}{2} \left(\frac{n_L}{n_H} + \frac{n_H}{n_L} \right) \sin^2 \beta \tag{18}$$

In Equation 18 we considered quarter-wave films and we draw our attention to the normal incidence case ($\theta_i = \theta_2 = \dots = \theta_t = 0^\circ$), that is $\beta = \beta_2 = \beta_3 = \pi/2$.

Note that from values of n_L and n_H in bi-layer stacks such as special dielectric mirror reported by Kohoutek et al. (2008) and omnidirectional mirror designed by Kim and Hwangbo (2002), Deopura, Ullal, Temelkuran and Fink (2001), Chen et al. (1999) and Fink et al. (1998), the term within brackets in Equation 18 is often greater than 2. As a result, α cannot exceed unity, but for some values of β the term α may become smaller than -1 , which means that $\cos^{-1}\alpha$ will be complex. This can be seen from the definition of the inverse cosine in terms of a natural logarithm, i.e.,

$$\cos^{-1}(z) = -i \ln(z + \sqrt{z^2 - 1}) = -i \ln(b e^{i\pi}) = -i \ln b + \pi \tag{19}$$

From the previous expression, we can see that the term in bracket of the natural logarithm is always negative for $z < -1$, which means that it can be expressed under the polar form as $b e^{i\pi}$. As b can be a fraction for z smaller than -1 , the imaginary part of $\cos^{-1}(z)$ can be fairly large. Therefore using simple trigonometry, it can be shown that $U_N(\alpha)$ have exponential behavior for $z < -1$ and can be very large. This leads to a high reflectance as the number N of periods increases. Finally, Equation (8) can be used to calculate the coefficient of reflection r for the quarter-wave bi-layer stack for the TM wave, provided we set:

$$\begin{aligned}
m_{11} &= AU_{N-1}(\alpha) - U_{N-2}(\alpha) \\
m_{12} &= BU_{N-1}(\alpha) \\
m_{21} &= CU_{N-1}(\alpha) \\
m_{22} &= DU_{N-1}(\alpha) - U_{N-2}(\alpha)
\end{aligned} \tag{20}$$

and replace Y_3 by $Y_t = n_t (\frac{\epsilon_o}{\mu_o})^{1/2} / \cos \theta_t$. Likewise, the transmission coefficient t can also be calculated using the previous definitions and Equation (9).

Figure 7 shows both the reflectance and the transmittance for a quarter wave bi-layer stacks of chalcogenide films that are used to produce dielectric mirrors such as those reported by Kohoutek et al. (2008). In Figure 7, we consider cases for $N=5$, $N=15$ and $N=50$ and we assumed $n_H = 3.31$, $n_L = 2.11$, $d_2 = 117nm$ and $d_3 = 183nm$. The refractive indices for n_H and n_L for each film forming the bi-layer as well as their numerical values for thicknesses d_2 and d_3 were obtained from the literature explored by Kohoutek et al. (2008). Note from values of n_H , n_L , d_2 and d_3 that were used to produce the curves in Figure 7, each film corresponds to a quarter-wave as the

product $\beta = (2\pi/\lambda)n_H d_2 \sim (2\pi/\lambda)n_L d_3 \sim \pi/2$ at $\lambda \sim 1550\text{nm}$. Therefore, the reflectance should reach a maximum near $\lambda = 1550\text{nm}$ and the transmittance should be reduced to a minimum as their sum must be equal to 1 based on the principle of energy conservation.

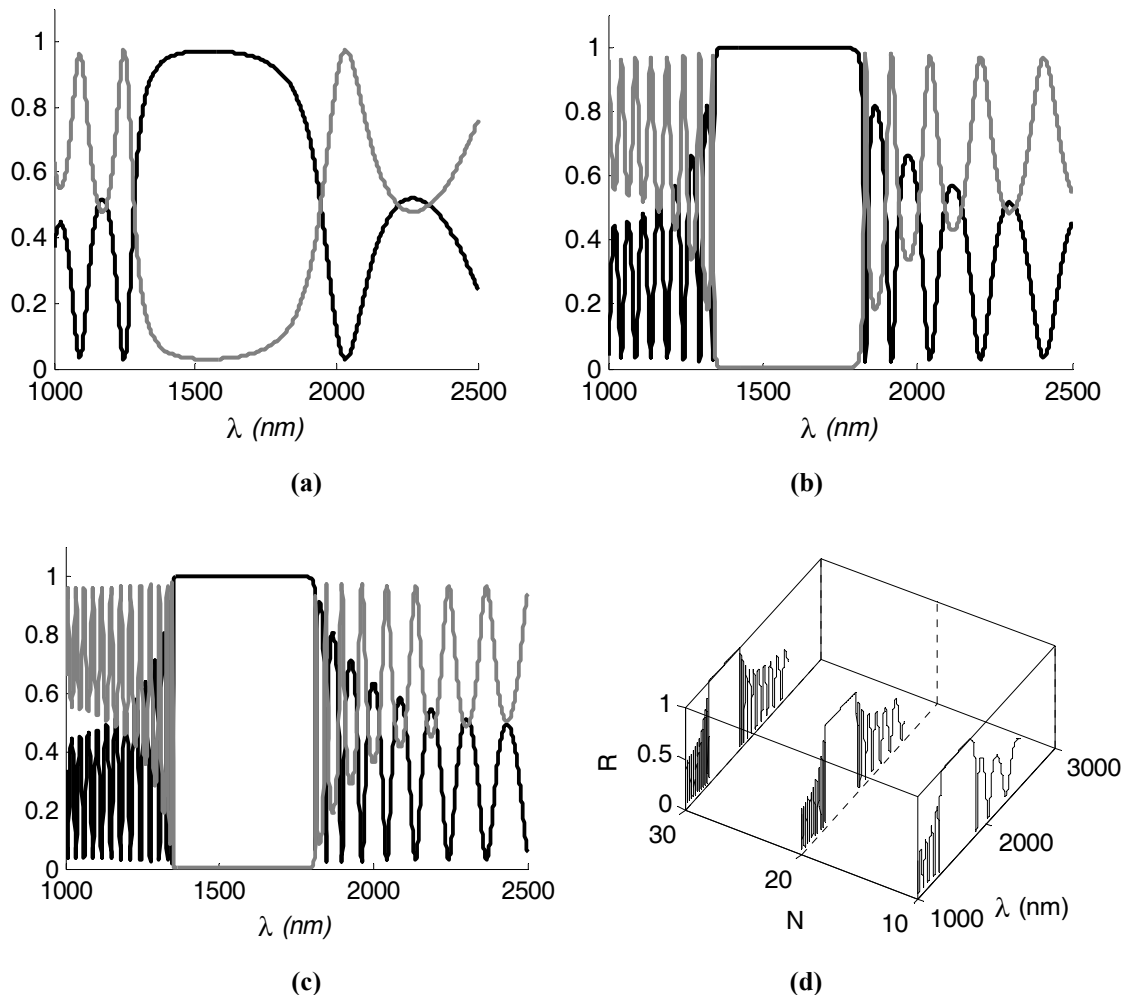


Figure 7. R (black line) and T (gray line) for a quarter-wave dielectric stacks of films. In the calculation, we used $n_H = 3.31$, $n_L = 2.11$, $d_2 = 117\text{nm}$, $d_3 = 183\text{nm}$. (a) $N = 5$, (b) $N = 15$, (c) $N = 25$ (d) Reflectance curve for $N = 10$, $N = 20$ and $N = 30$

From Figure 7, it can be seen that the reflectance curve (black curve) is approaching unity over a fairly large bandwidth centered on 1550nm . The bandwidth is looking as a top-hat shape-like Figure at $N=15$. For values of N greater than 15, no substantial change occurs regarding the spectral bandwidth, but more severe oscillations are appearing on either sides of the bandwidth window. In practice, an efficient dielectric mirror fabricated with 15 periods or so should meet the specification for most experiments.

2. Grating Waveguide Structures

In the previous section, we introduced systems involving homogenous thin films and presented a method to compute the reflectance and transmittance based on the matrix formalism. In this section, we will discuss some optical systems such as surface relief grating. In such systems the refractive index varies periodically along their surface within regions that are comparable to the incident light wavelength λ . Abrupt changes in reflectivity or transmission were first observed in gratings as early as 1902 by Wood (1902). These so-called anomalies in diffraction efficiency (DE) occurring over an angle range or a wavelength spectrum are very different from the normally smooth diffraction curves. These abrupt changes in DE led researchers to design and investigate resonant filters for applications in many devices including gratings.

Rigorous coupled wave analysis ($RCWA$) has been used extensively in the literature by Lenaerts et al. (2005),

Lalanne and Morris (1996) and Moharam et al. (1995) to calculate diffraction efficiencies (DE) in waveguide structures. In this section, the basic binary dielectric rectangular-groove grating is treated using the matrix formalism for the numerical method with careful considerations on the computation of DE for the TM wave. The results obtained for binary dielectric rectangular-groove grating are also applied to metallic grating. Introduction to photonic band gap systems are discussed and some examples are presented at the end of this section.

2.1 Mathematical Description of Binary Dielectric Gratings

Computations will be done for the TM wave on ridge binary grating bounded by two semi-infinite dielectric media of real permittivities ϵ_1 and ϵ_3 . The type of structures that will be presented in this section is based on the structure depicted in Figure 8. In the case of resonance reflection filters explored by Tibuleac and Magnusson (1997), the grooved region of permittivity ϵ_L and depth h is often filled by a material having a slightly lower permittivity than ϵ_H .

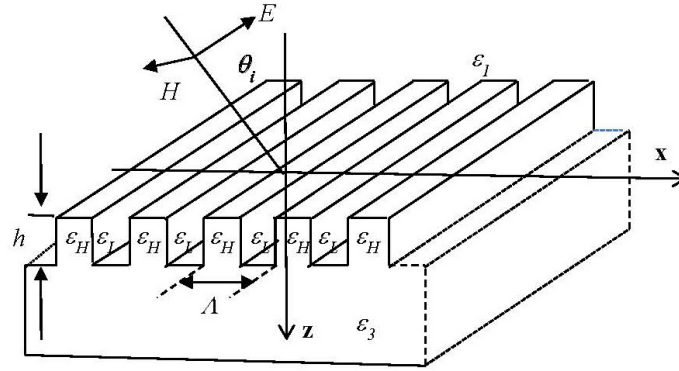


Figure 8. Basic structure of the binary rectangular-groove grating bounded by two semi-infinite dielectrics

The relative permittivity $\epsilon(x)$ of the modulated region shown in Figure 8 is varying periodically along the x -direction and is defined as:

$$\epsilon(x) = \sum \epsilon_s \exp(-2\pi j s x / \Lambda) \quad (21)$$

where ϵ_s is the s^{th} Fourier component of the relative permittivity in the grating region ($0 < z < h$), which can be complex in the case of metallic gratings. The incident normalized magnetic field that is normal to the plane of incidence (cf. Figure 8) is given by:

$$H_{inc,y} = \exp[-jk_o n_1 (\sin \theta_i x + \cos \theta_i z)] \quad (22)$$

where $k_o = 2\pi / \lambda$. θ_i is the incident angle with respect to the z -axis as shown in Figure 8.

The normalized solutions in regions 1 ($z < 0$) and 3 ($z > h$) are expressed as:

$$H_{1,y} = H_{inc,y} + \sum_i R_i \exp[-j(k_{xi} x - k_{1,zi} z)], \quad (23)$$

$$H_{3,y} = \sum_i T_i \exp[-j(k_{xi} x + k_{3,zi} (z - h))], \quad (24)$$

where k_{xi} is defined by the Floquet condition, i.e.,

$$k_{xi} = k_o (n_1 \sin \theta_i - i(\lambda / \Lambda)) \quad (25)$$

where i is an integer defining the order of the diffracted field into media 1 and 3.

Note that we also assumed the dependence $\exp(-j(\vec{k} \cdot \vec{r} - \omega t))$ as in section 1 for the sake of consistency. In previous equations, Λ is the grating spacing, $n_1 (\equiv \sqrt{\epsilon_1})$ is the refractive index of medium 1 and

$$k_{l,zi} = \left\{ \begin{array}{ll} k_o \left[n_l^2 - \left(\frac{k_{xi}}{k_o} \right)^2 \right]^{1/2} & k_o n_l > k_{xi} \\ -jk_o \left[\left(\frac{k_{xi}}{k_o} \right)^2 - n_l^2 \right]^{1/2} & k_{xi} > k_o n_l \end{array} \right\}, \quad (26)$$

with $l = 1, 3$. $n_3 (\equiv \sqrt{\epsilon_3})$ is the refractive index of medium 3.

R_i and T_i are the normalized electric-field amplitudes of the i^{th} diffracted wave in media 1 and 3, respectively. In the grating region ($0 < z < h$) the tangential magnetic (y -component) and electric (x -component) fields of the TM wave may be expressed as a Fourier expansion:

$$\begin{aligned} H_y &= \sum_i U_{yi}(z) \exp(-jk_{xi}x) \\ E_x &= j \left(\frac{\mu_o}{\epsilon_o} \right)^{1/2} \sum_i S_{xi}(z) \exp(-jk_{xi}x) \end{aligned} \quad (27)$$

where $U_{yi}(z)$ and $S_{xi}(z)$ are the normalized amplitudes of the i^{th} space-harmonic which satisfy Maxwell's equations, i.e.,

$$\begin{aligned} \frac{\partial E_x}{\partial z} &= -j\omega\mu_o H_y + \frac{\partial E_z}{\partial x} \\ \frac{1}{\epsilon(x)} \frac{\partial H_y}{\partial x} &= j\omega\epsilon_o E_z \end{aligned} \quad (28)$$

where ω is the angular optical frequency. ϵ_o and μ_o are respectively the permittivity and permeability of free space. As the $\exp(j\omega t)$ is used, all complex permittivity must be expressed under the form $\epsilon = \epsilon' - j\epsilon''$.

Substituting the set of Equations (27) into Maxwell's equations and eliminating E_z , the coupled-wave equations can be expressed in the matrix form as:

$$\begin{bmatrix} \partial U_y / \partial z' \\ \partial S_x / \partial z' \end{bmatrix} = \begin{bmatrix} 0 & E \\ B & 0 \end{bmatrix} \begin{bmatrix} U_y \\ S_x \end{bmatrix}, \quad (29)$$

where z' equals $k_o z$. In Equation (29), $B = K_x E^{-1} K_x - I$, E is the matrix formed by the permittivity elements, K_x is a diagonal matrix, with their diagonal entries being equal to k_{xm} / k_o and I is the identity matrix.

Matrix Equation (29) for a refractive-index profile of thickness h is analogous to matrix Equation (6) for a homogenous thin film. In matrix Equation (6), a 2×2 characteristic matrix is defined from the properties of the homogenous thin film such as its refractive index and thickness, whereas in Equation (29) a 2×2 block matrix is used to characterize the refractive index profile thickness.

Equation (29) under the matrix form can be reduced to

$$\left[\partial^2 U_y / \partial z'^2 \right] = [EB] [U_y] \quad (30)$$

Matrix Equation (30) is analogous to a second order differential equation with a known coefficient that can be obtained from a matrix product. Therefore, solutions of Equation (30) and the set of Equation (29) for the space harmonics of the tangential magnetic and electric fields in the grating region are expressed as:

$$\begin{aligned} U_{yi}(z) &= \sum_{m=1}^n w_{i,m} (c_m^+ \exp[-jk_o q_m z] + c_m^- \exp[jk_o q_m (z-h)]) \\ S_{xi}(z) &= \sum_{m=1}^n v_{i,m} (-c_m^+ \exp[-jk_o q_m z] + c_m^- \exp[jk_o q_m (z-h)]), \end{aligned} \quad (31)$$

where $w_{i,m}$ and q_m are the elements of the eigenvector matrix \mathbf{W} and the positive square root of the eigenvalues of matrix \mathbf{G} ($=-\mathbf{EB}$), respectively. The quantities c_m^+ and c_m^- are unknown constants (vectors) to be determined from the boundary conditions. The amplitudes of the diffracted fields R_i and T_i are calculated by matching the tangential electric and magnetic field components at the two boundaries. Using Equations (22), (23), (24) and (31) and the previously defined matrices, the boundary conditions at the input boundaries ($z = 0$ and $z = h$) are:

$$\begin{aligned} \delta_{i,0} + R_i &= Wc^+ + WXc^- \\ \frac{j \cos \theta}{n_1} \delta_{i,0} - jZ_1 R_i &= Vc^+ - VXc^- \end{aligned} \quad z = 0 \quad (32)$$

and

$$\begin{aligned} WXc^+ + Wc^- &= T_i \\ VXc^+ - Vc^- &= jZ_3 T_i \end{aligned} \quad z = h \quad (33)$$

where \mathbf{X} and \mathbf{Z}_l are diagonal matrices with diagonal elements $\exp(-jk_o q_m h)$ and $k_{lzi}/(n_l^2 k_o)$, respectively. c^+ and c^- are vectors of the diffracted amplitude in the i^{th} order. From (29) and (31), it can be shown that

$$V = jE^{-1}WQ \quad (34)$$

where $v_{m,l}$ are the elements of the product matrix with \mathbf{Q} being a diagonal matrix with diagonal entries q_l . \mathbf{Z}_3 is the diagonal matrix with diagonal elements $k_{3zi}/(n_3^2 k_o)$. Multiplying each member of the first equation in set of Equation (33) by $-j\mathbf{Z}_3$ and using the second equation to eliminate T_i vectors c^- and c^+ are related by:

$$c^- = (jZ_3W + V)^{-1}(-jZ_3W + V)Xc^+ \quad (35)$$

The main difference with homogenous thin film defined in section 1 is that a numerical solution is sought for the type of structure illustrated in Figure 8, which is a grating with a permittivity-index profile of high (ϵ_H) and low (ϵ_L) dielectric constant with a period Λ . Therefore, we must express one of the vectors c^+ or c^- in terms of known eigenvalues or eigenvectors that is characterizing that particular grating.

Multiplying each member of the first equation in set of Equation (32) by jZ_1 and using the second one to eliminate R_i a numerical computation can be found for c^+ by making used of Equation (35), that is:

$$c^+ = C^{-1} \left(\frac{j \cos \theta}{n_1} + jZ_1 \right) \delta_{i,0} \quad (36)$$

where

$$C = [(jZ_1W + V) + (jZ_1W - V)X(jZ_3W + V)^{-1}(-jZ_3W + V)X] \quad (37)$$

Note in Equation (36) that $\delta_{i,0}$ is a column vector. In the case of a solution truncated to the first negative and positive orders,

$$\delta_{i,0} = \begin{bmatrix} 0 \\ 1 \\ 0 \end{bmatrix} \quad (38)$$

assuming the incident wave to be a plane wave. In this particular case

$$\left(\frac{j \cos \theta}{n_1} + jZ_1 \right) \delta_{i,0} = \begin{bmatrix} 0 \\ j \frac{\cos \theta}{n_1} + jZ_1(2,2) \\ 0 \end{bmatrix}, \quad (39)$$

where $Z_1(2,2)$ is the element on line 2 and column 2 of matrix Z_1 . Finally, the vector on the right-hand side of Equation (39) is applied to the inverse matrix of C ($=C^{-1}$) to find the column vector for the diffracted amplitude

c^+ from Equation (36). Then c^- is found from Equation (35) and the normalized electric field amplitudes for R_i and T_i can be found from Equations (32) and (33). Only the DE in reflection and transmission for zeroth order are computed in the examples that will be discussed throughout this section. The diffraction efficiencies in both reflection (DE_R) and transmission (DE_T) are defined as:

$$DE_r = R_0 R_0^* \operatorname{Re}(k_{1,z0} / (k_o n_1 \cos \theta_i)) \tag{40}$$

and

$$DE_t = T_0 T_0^* \operatorname{Re}\left(\frac{k_{3,z0}}{n_3^2}\right) / \left(\frac{k_o \cos \theta_i}{n_1}\right). \tag{41}$$

2.2 Examples with Binary Dielectric Periodic Gratings

Let us consider a binary rectangular-groove grating with real permittivity ϵ_L and ϵ_H as shown in Figure 8. In the case of notch filters reported by Bertoni, Cheo, and Tamir (1989), Wang, Magnusson, Bagby and Moharam (1990), Gale, Knop and Morf (1990) and Peng and Morris (1996), the higher permittivity value ϵ_H ($\Lambda / 2 < x < \Lambda$) is slightly greater than ϵ_L ($\Lambda < x < \Lambda / 2$). Figure 9 shows the numerical computation for DE from the *RCWA* formulation for the *TM* wave when only three orders ($m = -1, 0, 1$) are retained in the computation at normal incidence.

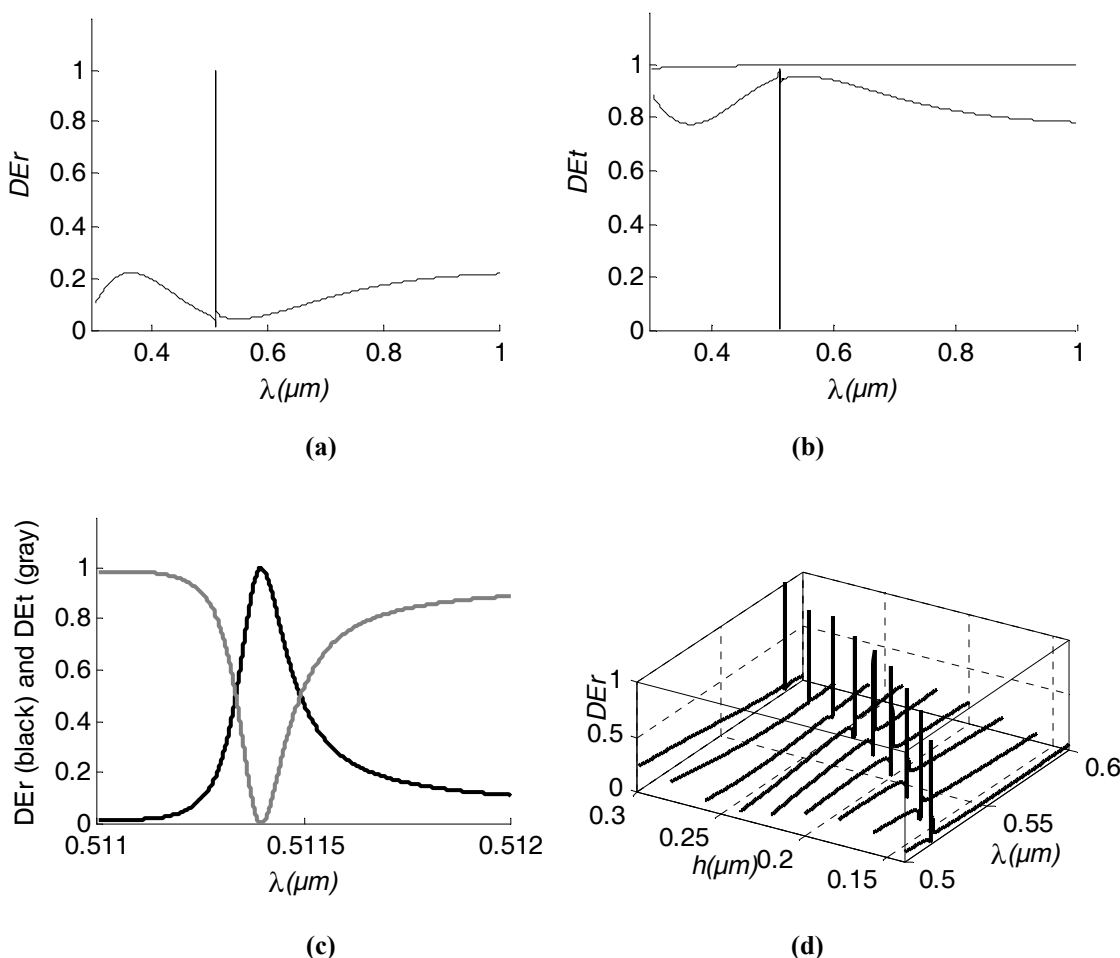


Figure 9. Diffraction efficiencies in reflection (DE_r) and transmission (DE_t) for the grating structure shown in Figure 8 at normal incidence. The following data were used to produce the numerical computations: $\epsilon_H = 4.41$, $\epsilon_L = 4.00$, $\Lambda = 0.314 \mu\text{m}$, $h = 0.134 \mu\text{m}$, $\epsilon_1 = 1.00$ (air) and $\epsilon_3 = 2.31$. a) DE_r displaying a very sharp peak near $\lambda = 0.512 \mu\text{m}$ b) DE_t and the sum of DE_r and DE_t within the spectral range 0.3-1.0 μm . c) DE_r and DE_t within a very small spectral range. d) DE_r at various thicknesses h . All other values afore-mentioned were kept the same

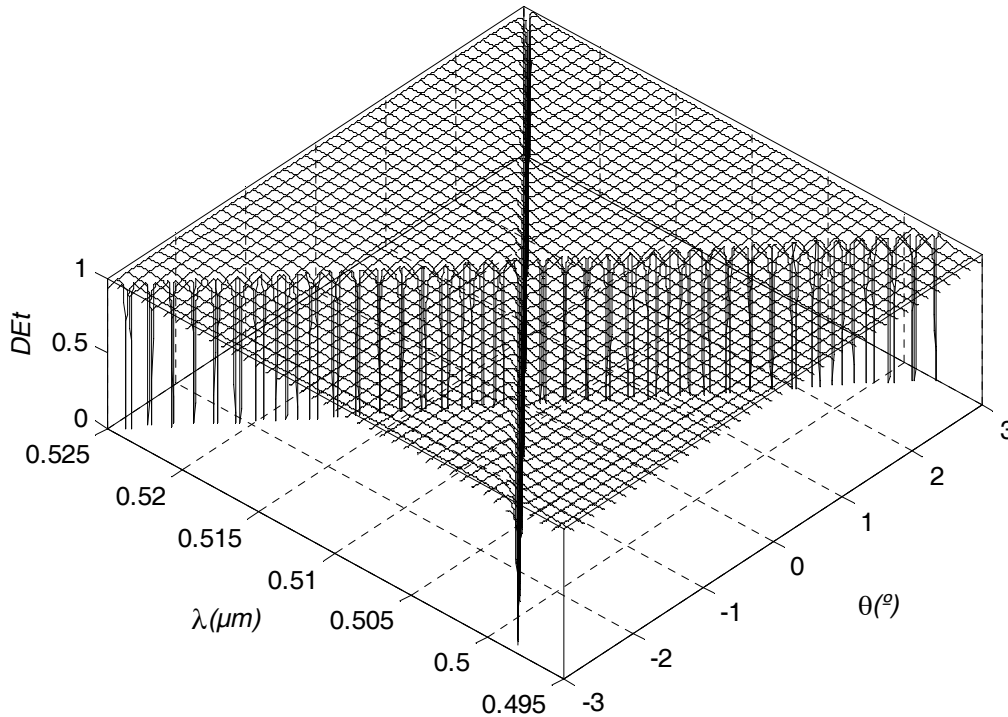


Figure 10. 3D plot of diffraction efficiencies in transmission (DE_t). The following data were used to produce the numerical computations: $\epsilon_H = 4.41$, $\epsilon_L = 4.00$, $\Lambda = 0.314 \mu\text{m}$, $h = 0.134 \mu\text{m}$, $\epsilon_1 = 1.00(\text{air})$ and $\epsilon_3 = 2.31$

The very sharp spike displayed in the DE_r curve in Figure 9(a) has an $FWHM$ smaller than 1 nm. This $FWHM$ is much smaller than the bandwidth of bilayer stack shown in Figure 7. The reflectance curve for the bi-layer dielectric stacks were also displaying large oscillation on either sides of the bandwidth centered on 1550 nm. Note that there are very few oscillations within the spectral range shown in Figure 9(a). Figure 9(b) is showing DE_t for the grating structure, which is also displaying a very sharp dip with a very small $FWHM$. The sum of DE_r and DE_t is also shown to be equal to 1 on most on the spectral range, which means that truncating the solution to the first positive and negative orders $m = -1, 0, 1$ is sufficient to yield enough accuracy for the numerical computation. The sum of DE_r and DE_t is slightly below 1 at shorter wavelengths and some more orders would be required to obtain a better accuracy in the numerical computation for $\lambda < 0.4 \mu\text{m}$. Figure 9(c) is showing DE_r and DE_t within a nanometer spectral range to appreciate the small $FWHM$ and Figure 9(d) is displaying DE_r for various thickness h to see by how much the peak is shifted along the spectral axis. Figure 10 shows a 3D plot of DE_t curves that meet at a single value of incident angle of 0° near $\lambda \sim 510 \text{ nm}$. Note the symmetry of each curve of DE_t for incident angles that are different from normal incidence. As the incident angle approaches normal incidence, the two dips at $\pm\theta_i$ are getting closer to collapse at normal incidence near $\lambda \sim 510 \text{ nm}$. Therefore the DE_t curves are forming two valleys which are crisscrossing and display a photonic band. This concept will be used in the next sections when photonic band gap are introduced.

2.3 Examples with Metallic Periodic Gratings

The theory presented in section 3.1 can be applied to metallic periodic gratings. For the TM wave many terms need to be retained in the numerical calculation to reach convergence as discussed by Li and Haggans (1993). Metallic periodic gratings are used to excite surface plasmons (SP) to improve Surface-enhanced-Raman-Scattering (SERS) sensor performances as reported by Sheng, Stepleman and Sanda (1982). Substituting Equation (21) and Equation (31) into Maxwell's Equations (28) and eliminating E_z , it can be shown that

$$\frac{\partial S_{xm}}{\partial z'} = j \left(\sum_p \frac{k_{xm}}{k_o} \epsilon_{i-p}^{-1} \frac{k_{xm}}{k_o} U_{yp} - U_{yi} \right). \quad (42)$$

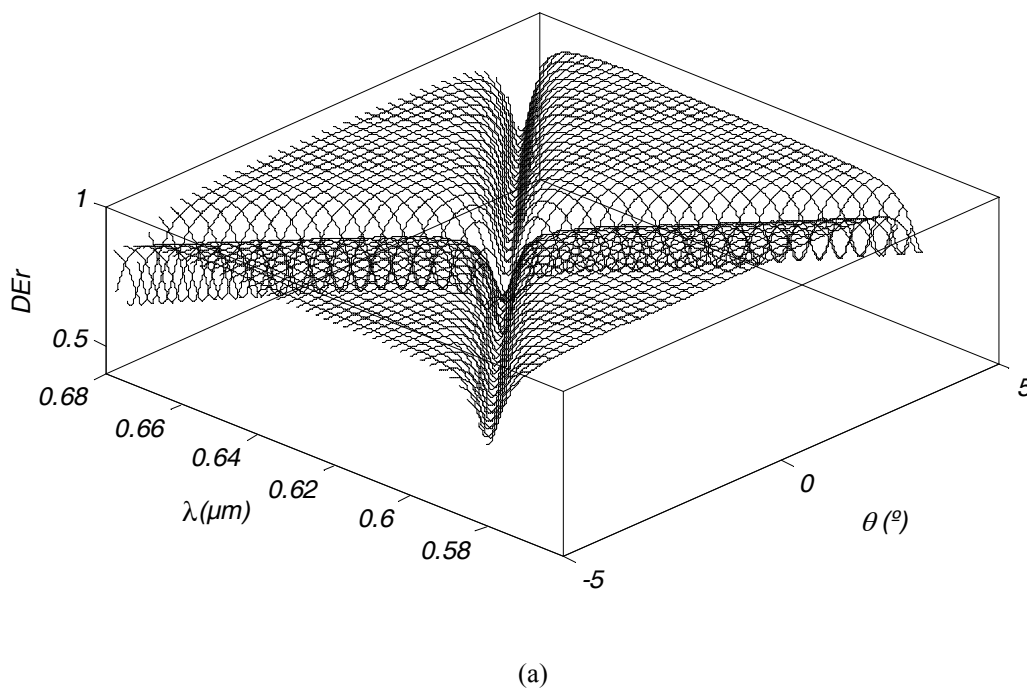
Equation (42) is one of the two coupled-wave equations involving the inverse permittivity for the case of TM polarization only. In the conventional formulation by Moharam and Gaylord (1981) and Moharam et al. (1995), the term ϵ_{i-p}^{-1} is treated by taking the inverse of the matrix \mathbf{E} defined by the permittivity components, with the i ,

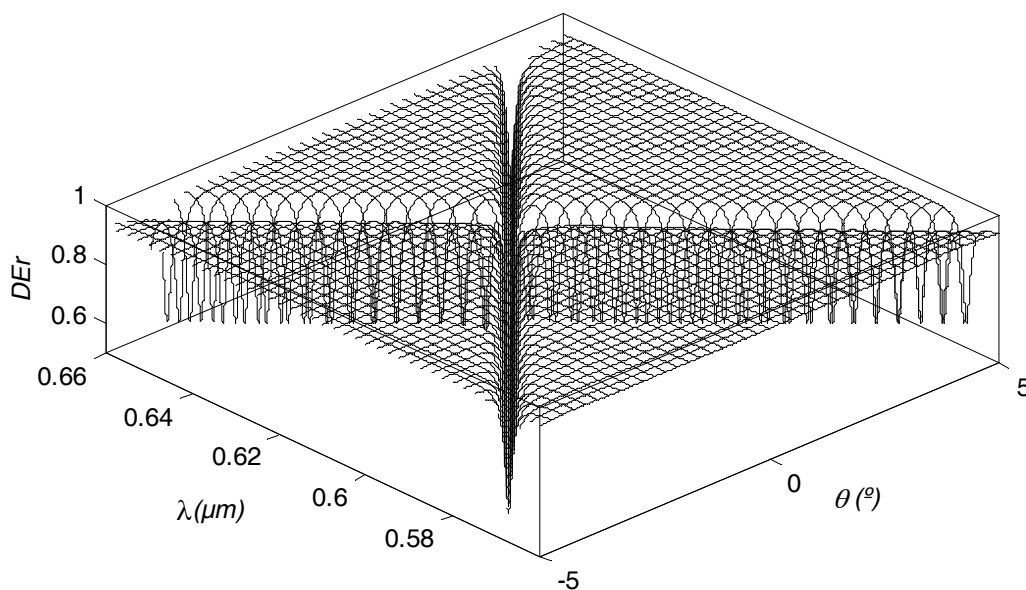
p elements being equal to $\varepsilon_{(i-p)}$. In the reformulation of the eigenvalue problem by Lalanne and Morris (1996), the term ε_{i-p}^{-1} is considered in a different manner by forming a matrix A of the inverse-permittivity coefficient harmonics for the two regions ($1/\varepsilon_H$ and $1/\varepsilon_L$) inside the modulated region. Fourier expansion in Equation (21) is modified to:

$$1/\varepsilon(x) = \sum_s \left(1/\varepsilon_s\right) \exp(-2\pi j s x / \Lambda) \quad (43)$$

where $(1/\varepsilon)_s$ is the s^{th} Fourier component of the relative permittivity in the grating region. It was shown that this reformulation of the eigenvalue problem is converging more quickly than the conventional method as much less terms are required in the numerical computation.

Since the coupled-wave equations do not involve the inverse of the permittivity in the coupled-wave equations for the TE wave, matrix A is not needed in numerical computations and the eigenvalue problem is greatly simplified in this case. As a result, solutions for the TE wave are more stable in metallic lamellar gratings. The theory presented earlier in sections 2i) and 2ii) is still applied to metallic periodic gratings, but the Fourier expansion in Equation (43) will be used instead to obtain faster convergence of the eigenvalue problem. For the sake of saving time a fairly accurate computation is reached after retaining ten orders. Figure 11 shows DE_r for a metallic periodic grating using a 3D plot. This 3D plot is similar to Figure 10 for a binary dielectric grating except the $FWHM$ is larger as a complex value is assumed for the metal. At a given wavelength λ the reflectivity of the metallic grating should be symmetric with the incident angle θ . If a reflectivity drop occurs due to SP at θ , the metallic periodic grating should display a similar drop at $-\theta$. Note that two minima occur on either side of normal incidence ($\theta = 0^\circ$) and one single minimum is displayed at normal incidence for $\lambda \sim 630$ nm. Basically each minimum in DE_r forms two valleys which crisscross at normal incidence and $\lambda \sim 630$ nm. Essentially, the 3D plots shown in Figures 10 and 11 would be forming a band in k -space as pointed out by Barnes, Priest, Kitson and Sambles (1996) and demonstrated by Lévesque and Rochon (2005). From Figure 11, two bands appear to be meeting at a common value of incident angle and wavelength. Note that the $FWHM$ of each dip depends strongly upon the metal dielectric constant as shown in Figures 11(a) and 11(b) for gold and silver, respectively.





(b)

Figure 11. 3D plots of DE_r for a periodic metallic grating. In the calculation, we used $\varepsilon_I = 1$, $\Lambda = 600 \text{ nm}$ and $h = 10.5 \text{ nm}$. a) gold with $\varepsilon_L = -10.7-j$, $\varepsilon_H = 1$ and $\varepsilon_3 = -10.7-j$ b) silver $\varepsilon_L = -17.7-0.7j$, $\varepsilon_H = 1$ and $\varepsilon_3 = -17.7-0.7j$

2.4 Single and Double Metallic Corrugated Surfaces

Double metallic corrugated surfaces have been produced to generate a band gap. In some cases, the surface becomes corrugated in a periodic fashion and looks as a superposition of two sine waves having a different harmonic component as described by Barnes, Priest, Kitson and Sambles (1996) and Lévesque and Rochon (2005). The surface profile $s(x)$ shown in the atomic microscope image in Figure 12 can be represented as

$$s(x) = h_1 \sin(K_1 x) + h_2 \sin(K_2 x + \phi_2) \quad (44)$$

where x is the spatial coordinate, h_1 and h_2 are the amplitudes of the two harmonic components K_1 and K_2 , and ϕ_2 is their relative phase. The harmonic components K_1 and K_2 are expressed as $2\pi/\Lambda_1$ and $2\pi/\Lambda_2$, respectively, where Λ is referred to as the grating pitch.

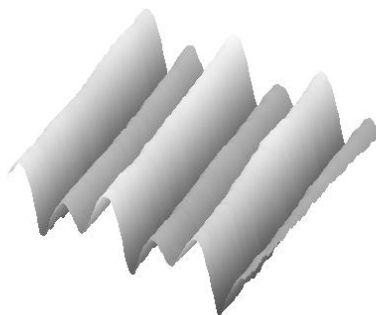


Figure 12. Atomic force microscope image of a double metallic Au grating. The pitches here are 700 and 375 nm with their respective depths of $19 \pm 1 \text{ nm}$ and $7.0 \pm 0.5 \text{ nm}$

In the case of a single grating with a harmonic component K_1 , the 3D plot of DE_r is shown in Figure 13(a) and looks very much like those obtained from numerical computation in Figure 11. Note that the signals obtained for the TM wave were normalized to that obtained for the TE wave. This was done as DE_r for the TE was showing

no minimum of reflection. The signal ratio was defined as R_p/R_s . In the case of a double grating surface with two harmonic components such as the one shown in Figure 12, the two photonic bands are no longer meeting at a common point near 0° and near $\lambda \sim 750$ nm as they open as shown in Figure 13(b). Clearly, a photonic gap is observed by superposing two gratings with different harmonic components.

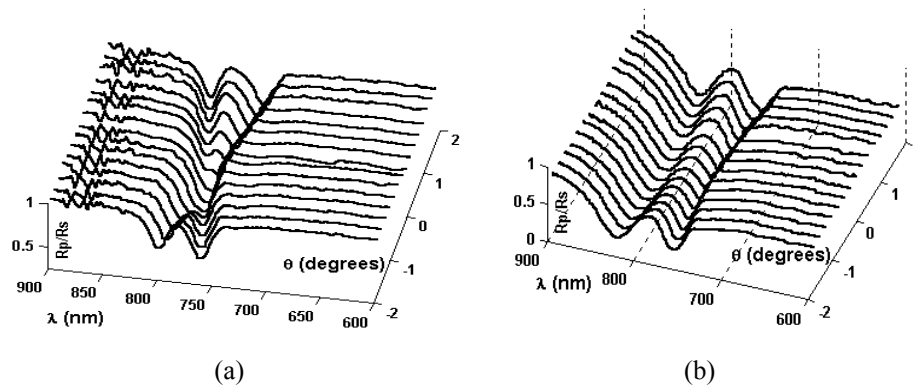


Figure 13. (a) Normalized reflectance (R_p/R_s) curve for a single gold grating with $\lambda \sim 755$ nm; (b) Normalized reflectance curve for a double metallic grating with $\lambda_1 \sim 755$ nm and $\lambda_2 \sim 375$ nm

The modulated films were made by holographic technique to write surface relief structures as reported by Lévesque and Rochon (2005). One grating is carefully written to have a spacing vector K_2 to generate a band gap in the SP dispersion curve. A second grating with grating spacing vector K_1 is superimposed and allows the coupling of the incident light to generate the SP itself. The grating with the second order (K_2 in this case) is therefore at the origin of the gap seen in the doubly corrugated surface shown in Figure 13(b).

3. Conclusion

The matrix formalism was shown to be efficient to predict the reflectance curve of both uniform films and periodic corrugated surfaces. It was shown that the reflectance derived from the matrix formalism is a method that describes precisely many optical thin film systems and grating structures. In some cases, the matrix formalism can be used to generate function curves that can be fitted to experimental data points. It was also shown that the matrix formalism can be used in numerical techniques and can be applied to periodic gratings to predict diffraction efficiencies.

Acknowledgement

This work is supported by the Academic research Program (ARP) at the Royal Military College of Canada.

References

- Abelès, F. (1950). Recherches sur la propagation des ondes électromagnétiques sinusoïdales dans les milieux stratifiés. Applications aux couches minces. *Ann. Phys., Paris*, 5, 596-640.
- Abelès, F. (1957). Optical Properties of Thin Absorbing Films. *J. Opt. Soc. Am.*, 47(6), 473-482, <http://dx.doi.org/10.1364/JOSA.47.000473>
- Barnes W. L., Priest T. W., Kitson S. C., & Sambles J. R. (1996). Physical origin of photonic energy gaps in the propagation of surface plasmons on gratings. *Phys. Rev. B*, 54(9), 6227-6244. <http://dx.doi.org/10.1103/PhysRevB.54.6227>
- Bertoni, H., Cheo, L., & Tamir, T. (1989). Frequency-selective reflection and transmission by a periodic dielectric layer, *IEEE Trans. Antenna Propag*, 37(1), 78-83. <http://dx.doi.org/10.1109/8.192167>
- Born, M., & Wolf, E. (1980). *Principles of Optics* (6th ed.), Cambridge: Cambridge University Press.
- Burke, J. J., Stegeman, G. I., & Tamir, T. (1986). Surface-polariton-like waves guided by thin, lossy metal films. *Phys. Rev B*, 33(8), 5186-5201. <http://dx.doi.org/10.1103/PhysRevB.33.5186>
- Chen, K. M., Sparks, A. W., Luan, H-C, Lim, D. R., Wada, K., & Kimerling, L. C. (1999). SiO₂/TiO₂ omnidirectional reflector and micro-cavity resonator via the sol-gel method, *Appl. Phys. Lett.*, 75(24), 3805-3807. <http://dx.doi.org/10.1063/1.125462>
- Deopura, M., Ullal, C. K., Temelkuran, B., & Fink, Y. (2001). Dielectric omnidirectional visible reflector. *Opt.*

- Lett.* 26(15), 1197-1199. <http://dx.doi.org/10.1364/OL.26.001197>
- Fink, Y., Winn, J. N., Fan, S., Chen, C., Michel, J., Joannopoulos, J. D., & Thomas, E. L. (1998). A dielectric omnidirectional reflector. *Science*, 27, 282(5394), 1679-1682. <http://dx.doi.org/10.1126/science.282.5394.1679>
- French, A. P. & Taylor, E. F. (1978). *An Introduction to Quantum Physics*. New York, NY: W.W. Norton & Company Inc.
- Gale, M. T., Knop, K., & Morf, R. H. (1990). Zero-order diffractive micro-structures for security applications in Optical Security and Anticounterfeiting Systems. Fagan W. F., (Ed.), *Proc. SPIE 1210*, 83-89.
- Haus, H. A. (1984). *Waves and fields in Optoelectronics, Prentice-Hall Series in Solid State Physical Electronics*. New Jersey: Englewood Cliffs.
- Heavens, O. S. (1960). Optical properties of thin films. *Rep. Prog. Phys.*, 23(1), 1-65.
- Hecht, E. (2002). *Optics* (4th ed.). New York, NY: Addison-Wesley.
- Homola, J., Yee, S. S., & Gauglitz, G. (1999). Surface Plasmons resonance sensors: review. *Sensors and Actuators B: Chem*, 54(1-2), 3-15. [http://dx.doi.org/10.1016/S0925-4005\(98\)00321-9](http://dx.doi.org/10.1016/S0925-4005(98)00321-9)
- Kano, H., & Kawata, S. (1994). Surface-plasmon sensor for absorption-sensitivity enhancement. *Appl. Opt.*, 33(22), 5166-5170. <http://dx.doi.org/10.1364/AO.33.005166>
- Kim, S.-H., & Hwangbo, C. K. (2002). Design of omnidirectional high reflector with quarter wave dielectric stacks for optical telecommunication bands. *Appl. Opt.* 41(16), 3187-3192. <http://dx.doi.org/10.1364/AO.41.003187>
- Kohoutek, T., Orava, J., Wagner, T., Hrdlicka, M., Vleck, M., & Frumar, M. (2008) Preparation of dielectric mirrors from high-refractive index contrast amorphous chalcogenide films. *J. Phys and Chem. Sol.*, 69(8), 2070-2074. <http://dx.doi.org/10.1016/j.jpcs.2008.03.003>
- Kovalenko, D. I. (1997). Voltage dependences of the amplitude and phase of reflected radiation in liquid-crystal structures with surface plasmons. *Tech. Phys. Lett.*, 23(9), 727-729. <http://dx.doi.org/10.1134/1.1261670>
- Lalanne, P., & Morris, G. M. (1996). Highly improved convergence of the coupled-wave method for TM polarization. *J Opt. Soc. Am. A*, 13(4), 779-784. <http://dx.doi.org/10.1364/JOSAA.13.000779>
- Lenaerts, C., Michel, F., Tilkens, B., Lion, Y., & Renotte, Y. (2005). High transmission efficiency for surface plasmon resonance by use of a dielectric grating. *Appl. Opt.*, 44(28), 6017-6022. <http://dx.doi.org/10.1364/AO.44.006017>
- Lévesque, L., & Rochon, P. (2005). Surface plasmon photonic bandgap in azopolymer gratings sputtered with gold. *J. Opt. Soc. Am. A*, 22(11), 2564-2568. <http://dx.doi.org/10.1364/JOSAA.22.002564>
- Lévesque, L. (2011a). *Electromagnetic Waves* (Chapter 12). In V. Zhurbenko (Ed.), Intech Open access publisher. <http://dx.doi.org/10.5772/693>
- Lévesque, L. (2011b). Determination of thickness and optical constants of metal films from an extended ATR spectrum by using a statistical method. *Optics & Laser Technology*, 43(1), 14-19. <http://dx.doi.org/10.1016/j.optlastec.2010.04.017>
- Lévesque, L., & Paton, B. E. (1994). Light switching in a glass-Ag-polymer structure using Attenuated total reflection (ATR). *Can. J. Phys.*, 72(9-10), 651-657. <http://dx.doi.org/10.1139/p94-084>
- Lévesque, L., & Paton, B. E. (1997). Detection of defects in multiple-layer structures by using surface plasmon resonance. *Appl. Opt.*, 36(28), 7199-7203. <http://dx.doi.org/10.1364/AO.36.007199> PMID:18264227
- Lévesque, L., Paton, B. E., & Payne, S. H. (1994). Precise thickness and refractive index determination of polyimide films using attenuated total reflection. *Appl. Opt.*, 33(34), 8036-8040. <http://dx.doi.org/10.1364/AO.33.008036>
- Li, L., & Haggans, C. W. (1993). Convergence of the coupled-wave method for metallic lamellar diffraction gratings. *J Opt. Soc. Am. A*, 10(6), 1184-1189. <http://dx.doi.org/10.1364/JOSAA.10.001184>
- Liboff, R. L. (1988). *Introductory Quantum Mechanics* (Chapter 7). Addison-Wesley Publishing Company Inc.
- Macleod, H. A. (2001). *Thin-film Optical Filters* (3rd ed.). Institute of Physics Publishing. <http://dx.doi.org/10.1201/9781420033236>
- Matsubara, K., Kawata, S., & Minami, S. (1988). Optical chemical sensor based on surface plasmon measurement.

- Appl. Opt.*, 27(6), 1160-1163. <http://dx.doi.org/10.1364/AO.27.001160>
- Moharam, M. G., & Gaylord, T. K. (1981). Rigorous coupled-wave analysis of planar-grating diffraction. *J. Opt. Soc. Am A*, 71(7), 811-818. <http://dx.doi.org/10.1364/JOSA.71.000811>
- Moharam, M. G., Grann, E. B., Pommet, D. A., & Gaylord, T. K. (1995). Formulation for stable and efficient implementation of the rigorous coupled-wave analysis of binary gratings. *J. Opt. Soc. Am. A*, 12(5), 1068-1076. <http://dx.doi.org/10.1364/JOSAA.12.001068>.
- Nikolajsen, T., Leosson, K., & Bozhevolnyi, S. I. (2004). Surface plasmon-polariton based modulator and switches operating at telecom wavelength. *Appl. Phys. Lett.*, 85(24), 5833-5835. <http://dx.doi.org/10.1063/1.1835997>
- Ohta, K., & Ishida, H. (1990). Matrix formalism for calculation of electric field intensity of light in stratified multilayered films. *Appl. Opt.*, 29(13), 1952-1959. <http://dx.doi.org/10.1364/AO.29.001952>
- Peng, S., & Morris, G. M. (1996). Sub-nanometer linewidth resonant grating filters. *Optics and Micro-optics*, 5, OSA Technical Digest Series (Optical Society of America, Washington, D.C., 257-260).
- Podgorsek, R. P., & Franke, H. (2002). Selective optical detection of aromatic vapors. *Appl. Opt.*, 41(4), 601-608. <http://dx.doi.org/10.1364/AO.41.000601>
- Raether, H. (1988). *Surface Plasmons on Smooth and Rough Surfaces and on Gratings*. Berlin: Springer-Verlag.
- Salamon, Z., Macleod, H. A., & Tollin, G. (1997). Coupled Plasmon-Waveguide Resonators; A new spectroscopic tool for probing proteolipid film structure and properties. *Biophys. J.*, 73(5), 2791-2797. [http://dx.doi.org/10.1016/S0006-3495\(97\)78308-5](http://dx.doi.org/10.1016/S0006-3495(97)78308-5)
- Sheng, P., Stepleman, R. S., & Sanda, P. N. (1982). Exact eigenfunctions for square-wave gratings: Application to diffraction and surface-plasmon calculations. *Phys Rev B*, 26(6), 2907-2916. <http://dx.doi.org/10.1103/PhysRevB.26.2907>
- Smith, W., Fakhouri, H., Pulpytel, J., & Arefi-Khonsari, F. (2012). Control of the optical and crystalline properties of TiO₂ in visible-light active TiO₂/TiN bi-layer thin-film stacks. *J. Appl. Phys.*, 111(2), 024301. <http://dx.doi.org/10.1063/1.3671428>
- Tazawa, M., Okada, M., Yoshimura, K., & Ikezawa, S. (2004). Sol. Energy Mater. *Sol. Cells*, 84(1-4), 159-170. <http://dx.doi.org/10.1016/j.solmat.2004.02.043>
- Tibuleac, S., & Magnusson, R. (1997). Reflection and transmission guided-mode resonance filters. *J. Opt. Soc. Am. A*, 14(7), 1617-1626. <http://dx.doi.org/10.1364/JOSAA.14.001617>
- Wang, S. S., Magnusson, R., Bagby, J. S., & Moharam, M. G. (1990). Guided-mode resonances in planar dielectric-layer diffraction gratings. *J. Opt. Soc. Am. A*, 7(8), 1470-1474. <http://dx.doi.org/10.1364/JOSAA.7.001470>
- Wang, Y. (2003). Wavelength selection with coupled surface plasmon waves. *Appl. Phys. Lett.*, 82(24), 4385-4387. <http://dx.doi.org/10.1063/1.1582357>
- Welford, K. (1991). Surface plasmon-polaritons and their uses. *Opt. Quant. Elect.*, 23(1), 1-27. <http://dx.doi.org/10.1007/BF00619516>
- Wood, R. W. (1902). On a remarkable case of uneven distribution of light in a diffraction grating spectrum. *Phil. Mag.*, 4(24), 396-402. <http://dx.doi.org/10.1081/14786440209462857>
- Yeh, P., Yariv, A., & Hong, C-S. (1977). Electromagnetic propagation in periodic stratified media. *I. General theory*, *J. Opt. Soc. Am.*, 67(4), 423-437. <http://dx.doi.org/10.1364/JOSA.67.000423>

Copyrights

Copyright for this article is retained by the author(s), with first publication rights granted to the journal.

This is an open-access article distributed under the terms and conditions of the Creative Commons Attribution license (<http://creativecommons.org/licenses/by/3.0/>).